Journal of Solid State Chemistry 181 (2008) 2994–3004

Contents lists available at ScienceDirect

Journal of Solid State Chemistry

journal homepage: www.elsevier.com/locate/jssc

Phase and valence transitions in $Ba_2LnSn_xNb_{1-x}O_{6-\delta}$

Paul J. Saines [a], Brendan J. Kennedy [a,*], Bernt Johannessen [b], Sarah Poulton [c,d]

[a] School of Chemistry, The University of Sydney, Sydney, New South Wales 2006, Australia
[b] Australian Nuclear Science and Technology Organization, Menai, New South Wales 2234, Australia
[c] NIST Center for Neutron Research, 100 Bureau Drive, Gaithersburg, MD 20899-6102, USA
[d] Department of Materials and Engineering, University of Maryland, College Park, MD 20742, USA

ARTICLE INFO

Article history:
Received 16 May 2008
Received in revised form
8 July 2008
Accepted 10 July 2008
Available online 22 July 2008

Keywords:
Perovskite
Phase transition
Valence state
XANES

ABSTRACT

The structures of compounds in the perovskite series $Ba_2LnSn_xNb_{1-x}O_{6-\delta}$ (Ln = Pr and Tb and $x = 0, 0.1, 0.2, \ldots, 1.0$) have been examined using synchrotron X-ray and neutron diffraction. It was found that niobate members of both series feature full *B*-site cation ordering but that this order is lost with increasing x. X-ray absorption near-edge structure (XANES) and near-infrared spectroscopies indicate that the oxidation state of the lanthanide cations gradually changes from Ln^{3+} to Ln^{4+} with increased Sn^{4+} doping. This is believed to be the cause of the loss of *B*-site ordering. Least squares analysis of the XANES spectra suggests that the rate of the transformation of Ln^{3+} cations to the tetravalent state is such that the Pr series contains no oxygen vacancies while the Tb series may contain a very small amount of vacancies, with $\delta \approx 0.02$.

1. Introduction

Materials with the perovskite-type structure are of significant interest due to the wide range of interesting physical properties they exhibit [1]. One such property is the relatively high ionic and/or electronic conductivity exhibited by oxygen deficient perovskites [2–4]. High ionic and mixed ionic and electronic conductivity makes perovskites useful for application in solid oxide fuel cells (SOFCs), high-temperature oxygen separation, electrochemical reactors and oxygen sensors [2,5]. High ionic conductivity usually takes the form of either high oxygen anion conductivity, as found in $La_{1-x}Sr_xGaO_{3-\delta}$ [6] or proton conductivity such as in $BaCeO_{3-\delta}$ [7] or $Ba_2YSnO_{5.5}$ [8], and is usually associated with the presence of a significant number of oxygen vacancies. High electronic conductivity is often associated with cations adopting a mixture of valence states [3].

Clearly in compounds with a cation that has the potential to exhibit mixed valencies there is a relationship between the number of oxygen vacancies present and the amount of the mixed valence cation oxidised to the higher valence state. Therefore it is important to understand the relative stability of oxygen vacancies in the perovskite structure, compared to the oxidation of a cation capable of adopting a higher valency, because of the impact this will have on the conductivity of these materials. Recently work undertaken in our group has shown that in the series $Ba_2LnSn_xSb_{1-x}O_{6-\delta}$ (Ln = Pr or Tb) the Ln^{3+} cations undergo a change in valency to Ln^{4+} with increased Sn^{4+} doping such that there were little or no oxygen vacancies present in these compounds [9]. Studies, conducted by synchrotron X-ray and neutron diffraction, showed that the oxidation state changed from the trivalent to tetravalent state led to a loss of the *B*-site ordering in these double perovskites. Interestingly it was found that the Pr^{3+} and Pr^{4+} cations in the $Ba_2PrSn_xSb_{1-x}O_{6-\delta}$ series segregated into two different structures over a large composition range while the Tb^{3+} and Tb^{4+} cations were both contained in the same phase for all compositions. The reason for this difference is unclear and it is interesting to examine what effect a subtle change to these series will have on the oxidation state of the lanthanides, the structures of these materials and the presence of any phase segregation.

One possible subtle change is the replacement of Sb^{5+} with Nb^{5+} as the pentavalent cation in the perovskite series. These two cations have similar charge and size (cf. an ionic radius of 0.60 and 0.64 Å for Sb^{5+} and Nb^{5+} [10]) but it has been established that there is a significant difference in the structure and chemistry of perovskite-type materials containing these cations. There are numerous examples where the niobate and antimonate compounds adopt different structures or where the antimonate but not the corresponding niobate, or vice versa, forms. One such case is the series $Ba_2LnB'O_6$ (Ln = lanthanide and B' = Nb^{5+} or Sb^{5+}) where both the antimonate and niobate form, but these adopt different structures. Both series undergo a sequence of phase transitions with decreasing average ionic radii of the *B*-site cations from $I2/m$ monoclinic (Glazer tilt system $a^-a^-c^0$ [11,12]) to an

* Corresponding author. Fax: +61 2 9351 3329.
E-mail addresses: kennedyb@chem.usyd.edu.au, B.Kennedy@chem.usyd.edu.au (B.J. Kennedy).

0022-4596/$ - see front matter © 2008 Elsevier Inc. All rights reserved.
doi:10.1016/j.jssc.2008.07.021

intermediate structure and then ultimately to $Fm\bar{3}m$ cubic ($a^0a^0a^0$) symmetry [13]. The intermediate structure adopted by the two series is, however, different with the antimonates having a $R\bar{3}$ rhombohedral ($a^-a^-a^-$) intermediate while the majority of niobates adopt an $I4/m$ tetragonal ($a^0a^0c^-$) structure [13,14]. Since the Ba_2LnSbO_6 and Ba_2LnNbO_6 compounds are the $x=0$ end-members of the $Ba_2LnSn_xSb_{1-x}O_{6-\delta}$ and $Ba_2LnSn_xNb_{1-x}O_{6-\delta}$ series it was of interest to see what chemical and structural differences there may be between the tin-doped niobates and antimonates.

The structural and chemical features of the $Ba_2LnSn_xNb_{1-x}O_{6-\delta}$ family of compounds have been explored by synthesising two series; namely $Ba_2PrSn_xNb_{1-x}O_{6-\delta}$ and $Ba_2TbSn_xNb_{1-x}O_{6-\delta}$. These series were structurally characterised using a combination of synchrotron X-ray, and in selected cases, neutron diffraction, both at and, where appropriate, above room temperature. To more clearly elucidate the oxidation states of the cations, particularly the lanthanides, present in these compounds they have also been extensively examined using X-ray absorption near-edge structure (XANES) and UV-Visible and near-infrared spectroscopies. These techniques provide more accurate and precise methods for examining the oxidation states of the cations in a compound, and hence determining the extent of the oxygen deficiency.

2. Experimental

All materials were obtained from Aldrich Chemicals. The lanthanide oxides and barium carbonate were dried prior to use by heating overnight at 1000 and 100 °C, respectively. Samples of $Ba_2LnSn_xNb_{1-x}O_{6-\delta}$ (Ln = Pr and Tb and $x = 0, 0.1, 0.2, \ldots, 1$) were prepared from stoichiometric mixtures of $BaCO_3$, SnO_2, Nb_2O_5 and either Pr_6O_{11} or Tb_4O_7. The samples were finely ground as an acetone slurry and after being allowed to dry were heated at 1200 °C for 24 h. The samples were then heated again at 1300 °C for 24 h, reground, pelleted and then heated at 1350 °C for a total of 48 h. Where necessary the samples were then reheated, in pelleted form, at 1400 and 1450 °C for periods of 24 h. Samples were reground between all heating periods.

The reactions were monitored by powder X-ray diffraction using Cu-$K\alpha$ radiation on a Shimadzu S-6000 diffractometer. Synchrotron X-ray diffraction patterns for the final samples were recorded on the Debye Scherrer diffractometer at the Australian National Beamline Facility, beamline 20B at the Photon Factory, Tsukuba, Japan [15]. The samples were housed in 0.3 mm capillaries that were continuously rotated during measurement to reduce the effects of preferred orientation. Data were collected using three image plates as detectors covering the range of $5^\circ < 2\theta < 125^\circ$ with a step size of 0.01° and a wavelength of 0.80286(1) Å. Variable temperature measurements, at temperatures of up to 800 °C, were carried out for selected samples using a custom built furnace over a range of $5^\circ < 2\theta < 85^\circ$.

Ambient temperature neutron powder diffraction data of $Ba_2PrSn_xNb_{1-x}O_{6-\delta}$ ($x = 0$, 0.6 and 0.7) and $Ba_2TbSn_xNb_{1-x}O_{6-\delta}$ ($x = 0.3$, 0.6 and 0.7) were collected using the BT-1 32 detector neutron powder diffractometer at the NIST Center for Neutron Research reactor, NBSR. A Cu(311) monochromator with a 90° take-off angle, $\lambda = 1.5403(2)$ Å, and in-pile collimation of 15 min of arc were used. Data were collected over the range of 3° 2θ –168° 2θ with a step size of 0.05°. The instrument is described in the NCNR WWW site (http://ncnr.nist.gov/). A neutron powder diffraction pattern of Ba_2TbNbO_6 was collected using the high-resolution diffractometer, HRPD, at the HIFAR facility operated by the Australian Nuclear Science and Technology Organisation (ANSTO), Lucas Heights, Australia. A wavelength of 1.4924(1) Å was used to collect a pattern over a range of 10° 2θ–150° 2θ with a step size of 0.05° [16].

Refinements of the crystal structure were performed using the program RIETICA [17]. The diffraction peaks were described by a pseudo-Voigt function using a Howard asymmetry correction where necessary [17]. For neutron diffraction patterns the background was calculated using a six-parameter polynomial while for the X-ray patterns the background was estimated from interpolation between up to 40 selected points. It should be noted that the estimated standard deviations of variables determined by Rietveld refinement tend to underestimate the probable error in these values because they are based on random errors alone and do not include any systematic errors such as those in the wavelengths or models used [18,19].

XANES spectra of the Pr and Tb L_{III}-edges of both series were collected at beamline 20B at the Photon Factory over the range of 5.745–6.110 keV and 7.295–7.809 keV, respectively. A count time of 1 s per step with an energy step of 0.2 eV around each absorption edge was used. These measurements were conducted in transmission mode with the samples diluted, as appropriate, in BN and held between Kapton tape in a 1 mm thick sample holder. X-rays were monochromated using a channel cut Si(111) monochromator, which was detuned by 50% to reject higher harmonics. XANES spectra were measured using two ion chambers, one before and one after the sample. The incoming ion chamber was 31 cm long and filled with 30% N_2 in He while the transmitted ion chamber was 5 cm in length and filled with Ar. The energy of the Pr L-edge spectra was calibrated using the Cr K-edge of a 10% Cr in steel foil but the Tb spectra were not calibrated due to difficulties with the Co foil selected to be used as the reference for these samples. $Ln_2Sn_2O_7$ ($Ln = Pr^{3+}$ and Tb^{3+}) and $BaLnO_3$ ($Ln = Pr^{4+}$ and Tb^{4+}) were used as oxidation state standards for the trivalent and tetravalent oxidation states, respectively, as part of the analysis of the Pr and Tb L_{III}-edges. These compounds were synthesised in pure form using the methods of Kennedy et al. [20] for $Ln_2Sn_2O_7$ and Yoshimura et al. [21] and Hinatsu [22] for $BaLnO_3$. Subsequent to data collection the spectra were normalised using the BACKSUB procedure in EXAFSPAK [23]. Principal component, target transformation and multiple linear regression analyses of the XANES spectra were carried out using the PCA, TARGET and DATFIT programs in EXAFSPAK. The principal component and target transformation analysis were carried out over the energy ranges 5.902–6.200 keV for Pr and 7.425–7.800 keV for Tb. The multiple linear regression analysis was carried out over reduced ranges of 5.950–6.050 keV and 7.475–7.675 keV for Pr and Tb, respectively.

Ultra-violet, visible and near-infrared spectra of the samples were measured using a Cary 5E UV-Vis-NIR spectrometer equipped with a diffuse reflectance attachment. Scans were usually taken between 200 and 2500 nm, using a data interval of 0.667 nm and a scanning rate of 200 nm/min. Polytetrafluoroethylene (PTFE) was used as the background for baseline scans with a standard correction being applied.

3. Results and discussion

Characterisation of the compounds in the series $Ba_2LnSn_xNb_{1-x}O_{6-\delta}$ (Ln = Pr and Tb) will be presented in three sections. The first two will detail the structures of the Pr and Tb series while the final section examines the oxidation states of the lanthanides in these two series using a combination of UV-Visible and near-infrared spectroscopy and XANES.

3.1. Structures of $Ba_2PrSn_xNb_{1-x}O_{6-\delta}$

Synchrotron X-ray diffraction patterns indicate that, as reported previously [9,13], Ba_2PrNbO_6 and $Ba_2PrSnO_{6-\delta}$ adopt the fully B-site ordered $I2/m$ monoclinic and the disordered $R\bar{3}c$

rhombohedral structures, respectively (see Fig. S1 in Supplementary material). $Ba_2PrSnO_{6-\delta}$ has a smaller unit cell than Ba_2PrNbO_6 (cf. a volume of 76.84(3)–78.878(2) Å^3 for $Ba_2PrSnO_{6-\delta}$ and Ba_2PrNbO_6, respectively, when reduced to the size of the primitive cubic unit cell), despite the larger ionic radius of Sn^{4+} (0.69 Å [10]) compared to Nb^{5+} (0.64 Å [10]). This is similar to the previous finding that Ba_2PrSbO_6 has a larger unit cell size than $Ba_2PrSnO_{6-\delta}$ [9] and suggests that the dominant oxidation state of Pr in Ba_2PrNbO_6 is trivalent. Refinement against a neutron diffraction pattern of Ba_2PrNbO_6 yields an occupancy of the axial and equatorial oxygen sites of 99(2)% and 102(1)%, respectively consistent with a fully stoichiometric compound with respect to oxygen (see Fig. 1 for the quality of the fit). Assuming that Nb in this compound is pentavalent, which is consistent with the use of Nb_2O_5 as a starting material and synthesis being under oxidising conditions, it is reasonable to conclude that Pr in Ba_2PrNbO_6 adopts the trivalent oxidation state. It has previously been established that the Pr in $Ba_2PrSnO_{6-\delta}$ is tetravalent [9] and the presence of Pr in different oxidation states in the stannate and niobate compounds is likely to be a key factor contributing to the difference in *B*-site cation ordering in these two structures.

The synchrotron X-ray diffraction patterns of intermediate compounds in the series $Ba_2PrSn_xNb_{1-x}O_{6-\delta}$ showed that a series of phase transitions occurred (see Fig. S1). While the diffraction pattern of $Ba_2PrSn_{0.1}Nb_{0.9}O_{6-\delta}$ was well fitted by a model with $I2/m$ symmetry (R_p and R_{wp} of 6.3% and 6.0%, respectively) attempts to fit more Sn^{4+}-rich samples with such a model were unsuccessful. Diffraction patterns of samples with $x = 0.2$–0.4 revealed the presence of a two-phase mixture (see Fig. S1). The diffraction patterns of samples with $x = 0.5$–0.7 featured splitting consistent with rhombohedral symmetry (see Fig. S1) and these also had low angle *R*-point super-lattice peaks, the overlapping (111) and (100) Bragg reflections, at $\approx 9.3^\circ$ indicating *B*-site cation ordering. Evidently the compounds $x = 0.5$–0.7 adopt $R\bar{3}$ rhombohedral symmetry and these three diffraction patterns were satisfactorily fitted using models with this symmetry. Diffraction patterns of the compounds with $x = 0.8$ and 0.9 still featured splitting consistent with rhombohedral symmetry but no longer had any indication of the low angle *R*-point reflections indicating that, like $Ba_2PrSnO_{6-\delta}$, they are $R\bar{3}c$ rhombohedral.

Having established that the structures on either side of the two-phase region were $I2/m$ monoclinic and $R\bar{3}$ rhombohedral a combination of these two models was used to fit the $x = 0.2$–0.4 samples. Good fits were obtained to the diffraction patterns of these samples using this approach. The existence of the two-phase region can be interpreted in two ways. It is either caused by the discontinuous phase transition that is required a to occur between structures adopting these two space groups or indicates that there is some type of cation segregation occurring. To confirm which of these possibilities was correct a sample of $Ba_2PrSn_{0.2}Nb_{0.8}O_{6-\delta}$ was examined between 150 and 300 °C using synchrotron X-ray diffraction. Such an approach has previously been used in the related $Ba_2PrSn_xSb_{1-x}O_{6-\delta}$ [9] and $Ba_2LnNb_xSb_{1-x}O_6$ [24] series to establish the presence of phase segregation where other methods such as scanning electron microscopy and energy dispersive X-ray analysis failed. The diffraction patterns obtained showed that above 150 °C the sample is single-phase and adopts rhombohedral symmetry. This strongly suggests that the two-phase co-existence of monoclinic and rhombohedral symmetries in the $x = 0.2$–0.4 samples of $Ba_2PrSn_xNb_{1-x}O_{6-\delta}$ is caused by a discontinuous phase transition between these two symmetries and not cation segregation. This indicates that the behaviour of the $Ba_2PrSn_xNb_{1-x}O_{6-\delta}$ series is significantly different than that of the analogous Sb^{5+} series as both Pr^{3+} and Pr^{4+} exist in single-phase samples in the niobates while in the antimonates Pr^{3+} and Pr^{4+} preferentially segregate into two different phases over a significant composition range.

The decrease in the rhombohedral angle of $Ba_2PrSn_{0.2}Nb_{0.8}O_{6-\delta}$ with increasing temperature implies that the phase transition to $Fm\bar{3}m$ cubic symmetry would be expected to occur slightly above 300 °C (see Fig. 2). The square of the rhombohedral distortion (α-60) versus temperature is linear (see Fig. 3). Since the rhombohedral distortion is proportional to the square of the order parameter (Q^2) of the Landau-free energy expansion the transition between the rhombohedral and cubic phases in this compound must be tricritical in nature [25]. An extrapolation of the square of the rhombohedral distortion to zero suggests that the phase transition should occur at approximately 302(4) °C, just slightly above the maximum temperature investigated. That the phase transition is tricritical is not surprising since such transitions often occur between two perovskite structures and can be interpreted as indicating the presence of an additional nearby stable phase.

Refinements against synchrotron X-ray diffraction patterns indicate that the $Ba_2PrSn_xNb_{1-x}O_{6-\delta}$ compounds with $x = 0$–0.5

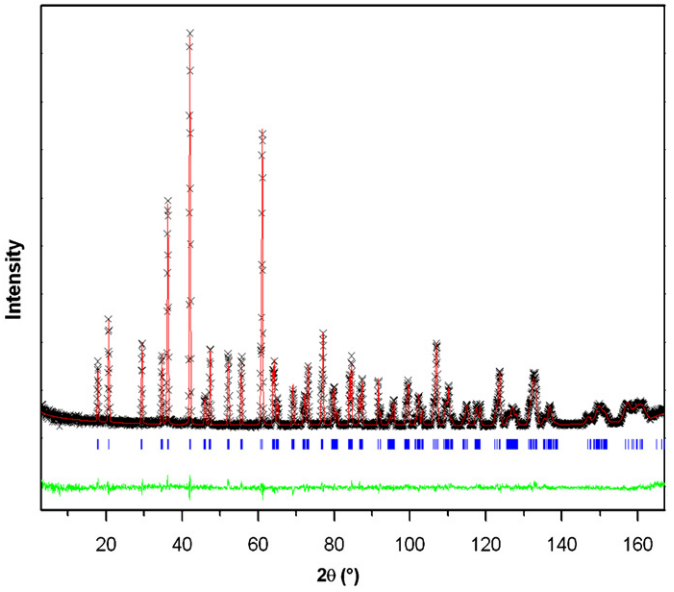

Fig. 1. Neutron diffraction pattern of Ba_2PrNbO_6 collected using a wavelength of 1.5403(2) Å. The crosses, upper and lower continuous lines represent the observed and calculated intensities and the difference between these, respectively. The vertical markers indicate the allowed Bragg reflections.

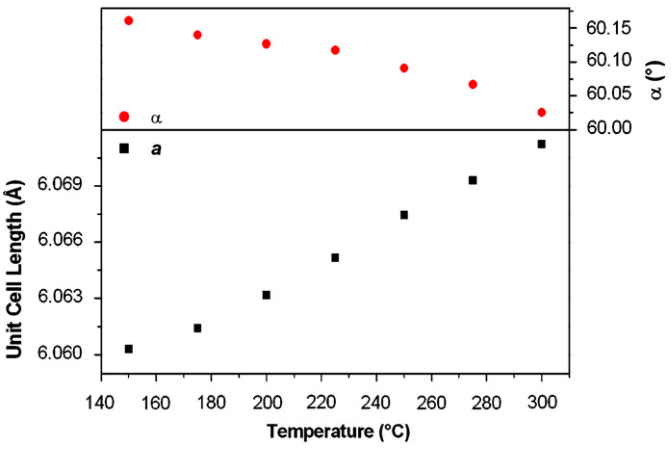

Fig. 2. Unit cell parameters of $Ba_2PrSn_{0.2}Nb_{0.8}O_{6-\delta}$ versus temperature.

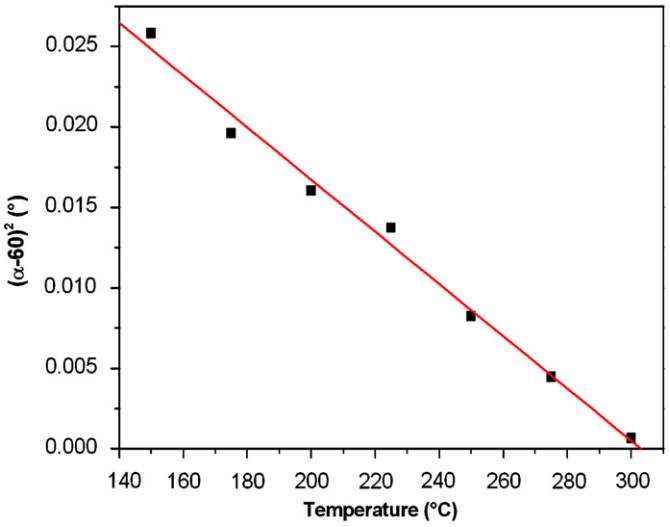

Fig. 3. Plot of the square of rhombohedral strain versus temperature for $Ba_2PrSn_{0.2}Nb_{0.8}O_{6-\delta}$. The linear nature of the plot confirms that the phase transition is tricritical.

have a high degree of *B*-site cation ordering with a minimum of approximately 90% Pr on the 2*a* and 1*a* sites (of the monoclinic and rhombohedral structures, respectively) with the other 10% being made up of Sn^{4+} and Nb^{5+} in a ratio fixed to the stoichiometry of the compound (the *B*′ site is fixed to have the opposite Pr and *B*′ ratio such as to maintain the nominal stoichiometry). Unfortunately, due to unusually high noise in the diffraction patterns of $x = 0.6$–0.7 samples it was not possible to reliably refine the degree of *B*-site cation ordering for these using X-ray diffraction. This high background was caused by air scattering due to instrumental failure and occurred despite two attempts to collect each pattern. In this case neutron diffraction is relatively sensitive to the degree of cation ordering of the Pr and *B*′ cations because of their different neutron scattering lengths (the coherent neutron scattering lengths of Nb, Sn and Pr are 7.14(3), 6.225(2) and 4.58(5) fm, respectively [26]). Refinement of neutron diffraction patterns of the $x = 0.6$ and 0.7 samples suggest that these samples are effectively fully ordered.

In contrast with the high degree of *B*-site cation ordering exhibited by the $x = 0$–0.7 samples, the $x = 0.8$ sample, $Ba_2PrSn_{0.8}Nb_{0.2}O_{6-\delta}$, adopts $R\bar{3}c$ symmetry indicating that a sudden loss of *B*-site cation ordering occurs between $x = 0.7$ and 0.8. On the other hand the Pr–O and Sn/Nb–O bond lengths in the compounds in the series $Ba_2PrSn_xNb_{1-x}O_{6-\delta}$ decrease and increase, respectively, in a gradual fashion with increasing *x* (see Tables 1 and 2 for crystallographic positions and cation bond distances, respectively). This occurs such that the Pr–O and Sn/Nb–O bond lengths have a small difference in length, ≈0.06 Å, in the $x = 0.7$ sample; the last sample before the *B*-site cations become completely disordered.

The evolution of Pr–O bond length is consistent with the gradual change in oxidation state from Pr^{3+} to Pr^{4+} across the series with the difference in Pr–O bond lengths between the Ba_2PrNbO_6 and $Ba_2PrSnO_{6-\delta}$ end-members being 0.20 Å. This change in Pr–O bond length is larger than the difference in the ionic radii of Pr^{3+} and Pr^{4+} (0.14 Å [10]) and this additional shortening of the Pr–O bond may be related to the Pr and Sn^{4+} cations sharing the same site in $Ba_2PrSnO_{6-\delta}$. Similarly to previous results for $Ba_2PrSn_xSb_{1-x}O_{6-\delta}$ the Pr cations are over-bonded throughout the series [9]. This is in contrast to the significant underbonding of Sn^{4+} and Nb^{5+}, particularly in the $x = 0.8$–1.0 samples where Pr, Sn^{4+} and Nb^{5+} all occupy the same crystallographic site. This suggests that there may be some local distortions around each of these different cations in the disordered structures to satisfy their different bonding requirements. Lattice parameters and unit cell volumes for compounds in the series $Ba_2PrSn_xNb_{1-x}O_{6-\delta}$ are illustrated in Fig. 4.

3.2. Structures of $Ba_2TbSn_xNb_{1-x}O_{6-\delta}$

As established by other studies Ba_2TbNbO_6 adopts an $I4/m$ tetragonal structure with full *B*-site cation ordering while the other end-member of the series, $Ba_2TbSnO_{6-\delta}$ exhibits $Pm\bar{3}m$ cubic symmetry and therefore has no *B*-site cation ordering [9,13]. Ba_2TbNbO_6 has a larger unit cell than $Ba_2TbSnO_{6-\delta}$ (cf. a reduced unit cell volume of 75.896(1)–73.9980(8) $Å^3$ for Ba_2TbNbO_6 and $Ba_2TbSnO_{6-\delta}$) suggesting that, similar to the Pr in $Ba_2PrSn_xNb_{1-x}O_{6-\delta}$, Tb undergoes a change of valence state with increasing *x*. Refinement of a suitable model against a neutron diffraction pattern of Ba_2TbNbO_6 indicates an occupancy of the oxygen anion equatorial and axial sites of 102(4)% and 100(2)% of full occupancy, respectively, indicating that Tb adopts the trivalent oxidation state in this compound (see Table 3 for crystallographic details). Since previous work established that $Ba_2TbSnO_{6-\delta}$ contains Tb^{4+} [9] it appears that the loss of *B*-site cation ordering between Ba_2TbNbO_6 and $Ba_2TbSnO_{6-\delta}$ is a consequence of the valency change of Tb^{3+} to Tb^{4+}. The degree of tetragonal splitting in Ba_2TbNbO_6 is quite small and a synchrotron X-ray diffraction pattern collected at 100 °C no longer contains any peak splitting suggesting that $Fm\bar{3}m$ cubic symmetry is adopted.

The synchrotron X-ray diffraction patterns of compounds in the series $Ba_2TbSn_xNb_{1-x}O_{6-\delta}$ with $x = 0.1$–0.3 feature splitting consistent with $I4/m$ symmetry. Subsequent refinements of models with this symmetry provide good fits to the data (see Fig. S2). The $x = 0.4$–0.9 members of the series do not have any peak splitting indicating that they adopt cubic symmetry analogous to $Ba_2TbSnO_{6-\delta}$ (see Fig. S2). The $x = 0.4$–0.6 compounds, however, feature weak *R*-point super-lattice reflections. Since these have cubic symmetry, and therefore lack any octahedral tilting, the *R*-point reflections arise from ordering of the *B*-site cations. These compounds adopt $Fm\bar{3}m$ cubic symmetry. The more Sn^{4+}-rich compounds ($x = 0.7$–0.9) do not show any *R*-point reflections confirming that they adopt the $Pm\bar{3}m$ structure displayed by $Ba_2TbSnO_{6-\delta}$.

The synchrotron X-ray diffraction patterns of the compounds in the series $Ba_2TbSn_xNb_{1-x}O_{6-\delta}$ with $x = 0.7$–1.0 feature peak asymmetry which increases at higher 2θ as was observed previously in the series $Ba_2TbSn_xSb_{1-x}O_{6-\delta}$ [9]. This asymmetry is similar to that noted in the peak shapes of the related compound Ba_2InNbO_6 by Ting et al. [27] which adopts the $Fm\bar{3}m$ cubic structure with a high degree of *B*-site cation disorder. Ting et al. postulated that this unusual peak shape is caused by strain induced by twinning and stacking faults resulting from disorder of the *B*-site cations. Since the *B*-site cations in the members of the series $Ba_2TbSn_xNb_{1-x}O_{6-\delta}$ with $x = 0.7$–1.0 are disordered it is likely that the peak shape observed in this compound is caused by a similar effect. Ting et al. [27] utilised a second $P4/mmm$ "phase" to account for the observed peak asymmetry and application of a similar model to the synchrotron X-ray diffraction patterns of the $x = 0.7$–1.0 samples in the $Ba_2TbSn_xNb_{1-x}O_{6-\delta}$ series results in a significant improvement in the quality of the fits. The peak shape parameters of this secondary phase are very broad confirming that the peak asymmetry is caused by strain in these compounds and not by the presence of a genuine second phase. Lattice parameters and unit cell volumes for compounds in the series $Ba_2TbSn_xNb_{1-x}O_{6-\delta}$ are plotted in Fig. 5.

Table 1
Crystallographic information for the series $Ba_2PrSn_xNb_{1-x}O_{6-\delta}$

x	0	0.2		0.6	0.7	0.8
Space group	$I2/m$	$I2/m$	$R\bar{3}$	$R\bar{3}$	$R\bar{3}$	$R\bar{3}c$
a (Å)	6.0940(1)	6.0849(1)	6.0443(2)	6.0336(3)	6.0278(3)	6.0209(2)
b (Å)	6.0546(2)	6.0510(1)	$=a$	$=a$	$=a$	$=a$
c (Å)	8.5521(2)	8.5495(2)	$=a$	$=a$	$=a$	$=a$
α (deg)	90	90	60.233(3)	60.127(4)	60.110(5)	60.052(3)
β (deg)	90.178(2)	90.130(1)	$=\alpha$	$=\alpha$	$=\alpha$	$=\alpha$
γ (deg)	90	90	$=\alpha$	$=\alpha$	$=\alpha$	$=\alpha$
Ba	4*i* (*x*,0,*z*)	4*i* (*x*,0,*z*)	2*c* (*x*,*x*,*x*)	2*c* (*x*,*x*,*x*)	2*c* (*x*,*x*,*x*)	2*a* ($\frac{1}{4}$, $\frac{1}{4}$, $\frac{1}{4}$)
x	0.5023(5)	0.4997(7)	0.2499(4)	0.2503(11)	0.2500	$\frac{1}{4}$
z	0.2476(5)	0.2489(4)	$=x$	$=x$	$=x$	$\frac{1}{4}$
B (Å^2)	0.81(2)	0.96(2)	1.31(5)	0.86(2)	0.86(2)	1.06(4)
Pr	2*a* (0,0,0)	2*a* (0,0,0)	1*a* (0,0,0)	1*a* (0,0,0)	1*a* (0,0,0)	2*b* (0,0,0)
B (Å^2)	0.72(5)	0.61(3)	1.33(7)	0.43(2)	0.50(2)	0.51(4)
B'	2*d* (0, 0, $\frac{1}{2}$)	2*d* (0, 0, $\frac{1}{2}$)	1*b* ($\frac{1}{2}$, $\frac{1}{2}$, $\frac{1}{2}$)	1*b* ($\frac{1}{2}$, $\frac{1}{2}$, $\frac{1}{2}$)	1*b* ($\frac{1}{2}$, $\frac{1}{2}$, $\frac{1}{2}$)	2*b* (0,0,0)
B (Å^2)	0.21(4)	0.55(4)	1.13(11)	0.45(2)	0.48(2)	= Pr B
O1	4*i* (*x*,0,*z*)	4*i* (*x*,0,*z*)	6*f* (*x*,*y*,*z*)	6*f* (*x*,*y*,*z*)	6*f* (*x*,*y*,*z*)	6*e* (x, $\frac{1}{2}-x$, $\frac{1}{4}$)
x	0.0537(4)	0.0470(20)	0.7138(44)	0.7385(11)	0.7433(16)	0.7858(10)
y	0	0	0.2313(38)	0.2247(5)	0.2240(5)	0.7142(10)
z	0.2698(3)	0.2555(24)	0.3381(28)	0.2876(5)	0.2827(7)	$\frac{1}{4}$
B (Å^2)	1.01(7)	0.89(17)	1.23(25)	1.82(2)	1.81(2)	0.88(9)
Occupancy	0.988(16)	1	1	0.998(4)	0.995(5)	1
O2	8*j* (*x*,*y*,*z*)	8*j* (*x*,*y*,*z*)				
x	0.2702(3)	0.2578(21)				
y	0.2669(4)	0.2698(25)				
z	0.9718(2)	0.9809(14)				
B (Å^2)	1.51(5)	1.29(19)				
Occupancy	1.015(10)	1				
R_p (%)	5.3	4.1		5.4	5.7	4.6
R_{wp} (%)	6.4	3.7		6.7	7.0	4.1
χ^2	1.0	57		1.6	1.9	46

Structures have been determined using either neutron or, in the case of the $x = 0.2$ and 0.8 samples, synchrotron X-ray diffraction. While the $x = 0$ and 0.2 samples have full *B*-site cation ordering the refinements of the 1*a* site in the $x = 0.6$ and 0.7 samples gives a Pr occupancy of 0.99(4) and 1.02(5). Standard uncertainties are given in parenthesis, and do not include uncertainty in the neutron wavelength used. It was not possible to stably refine the position of the Ba^{2+} cation in the $x = 0.7$ sample due to it oscillating either side of $\frac{1}{4}$. It was therefore set to this value.

Table 2
Bond lengths and bond valence sums (BVS) for selected compounds in the $Ba_2PrSn_xNb_{1-x}O_{6-\delta}$ series determined from refinements using neutron diffraction or, in the case of the $x = 0.8$ sample, synchrotron X-ray diffraction

x	Ba–O			Pr–O		B'–O	
	Bond length (Å)		BVS	Bond length (Å)	BVS	Bond length (Å)	BVS
0	1 × 2.741(4) 2 × 2.840(3) 2 × 2.884(4) 2 × 3.0500(5)	2 × 3.187(4) 2 × 3.246(4) 1 × 3.365(4)	1.79	2 × 2.329(2) 4 × 2.320(2)	3.61	2 × 1.997(2) 4 × 2.003(2)	4.70
0.6	3 × 2.833(1) 3 × 2.987(10)	3 × 3.059(10) 3 × 3.213(1)	1.77	6 × 2.196(4)	5.09	6 × 2.092(4)	3.62 3.67
0.7	3 × 2.842(1) 3 × 2.999(11)	3 × 3.039(11) 3 × 3.196(1)	1.77	6 × 2.169(5)	5.47	6 × 2.112(5)	3.43 3.49
0.8	3 × 2.7974(1) 6 × 3.018(6) 3 × 3.2283(1)		1.84	6 × 2.140(8)	5.91	= Pr–O	3.18 3.23

The BVS for Pr is based on the Pr^{3+}–O parameter since the appropriate value for Pr^{4+} is not known. In the case of the mixed Sn^{4+} and Nb^{5+} structures the BVS for Sn^{4+} is listed above Nb^{5+}.

Refinement of the structures in the $Ba_2TbSn_xNb_{1-x}O_{6-\delta}$ series against synchrotron X-ray diffraction patterns shows that the *B*-site cation ordering is lost gradually from full ordering in Ba_2TbNbO_6 to only 67.1(1) % of the 4*a* sites being occupied by Tb in $x = 0.6$. It should be noted that refinements of the partially ordered structures were done so as to maintain nominal stoichiometry. This gradual loss of *B*-site cation ordering is similar to the analogous antimonate series [9] but contrasts with $Ba_2PrSn_xNb_{1-x}O_{6-\delta}$ where cation ordering is suddenly lost between the $x = 0.7$ and 0.8 compounds. Consistent with the

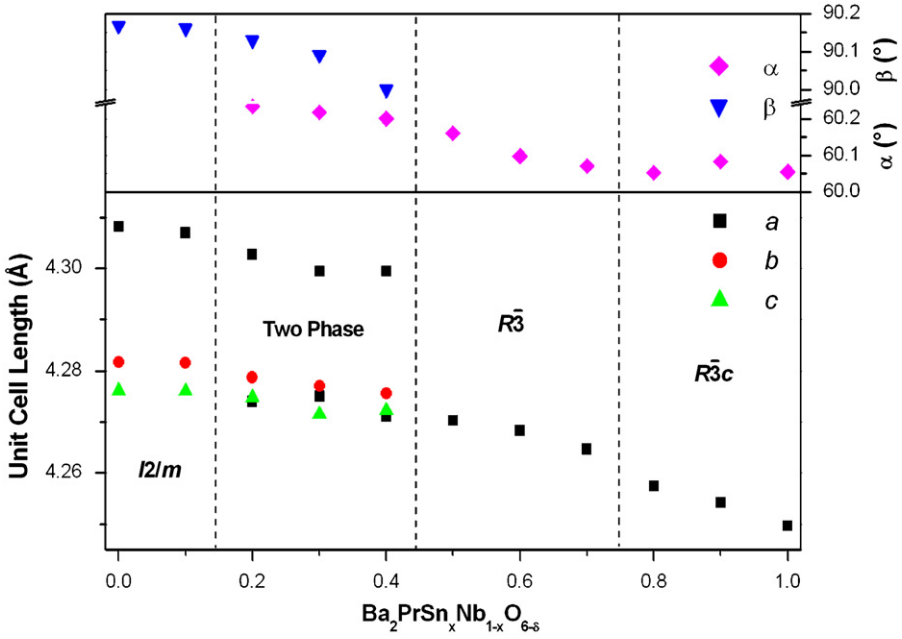

Fig. 4. Reduced unit cell parameters for compounds in the series $Ba_2PrSn_xNb_{1-x}O_{6-\delta}$.

Table 3
Unit cell parameters, atomic positions, displacements and oxygen occupancy parameters as determined using neutron diffraction for compounds in the series $Ba_2TbSn_xNb_{1-x}O_{6-\delta}$

Compound space group	Ba_2TbNbO_6 $I4/m$	$Ba_2TbSn_{0.3}Nb_{0.7}O_{6-\delta}$ $I4/m$	$Ba_2TbSn_{0.6}Nb_{0.4}O_{6-\delta}$ $Fm\bar{3}m$	$Ba_2TbSn_{0.7}Sb_{0.3}O_{6-\delta}$ $Pm\bar{3}m$
a (Å)	5.9816(1)	5.9796(3)	8.4364(2)	4.21390(8)
c (Å)	8.4757(2)	8.4588(10)	$=a$	$=a$
Ba	4*d* (0, $\frac{1}{2}$, $\frac{1}{4}$)	4*d* (0, $\frac{1}{2}$, $\frac{1}{4}$)	8*c* ($\frac{1}{4}$, $\frac{1}{4}$, $\frac{1}{4}$)	1*b* ($\frac{1}{2}$, $\frac{1}{2}$, $\frac{1}{2}$)
B (Å^2)	0.94(3)	0.69(2)	0.67(2)	0.71(2)
Tb	2*a* (0,0,0)	2*a* (0,0,0)	4*a* (0,0,0)	1*a* (0,0,0)
B (Å^2)	0.61(5)	0.23(6)	0.37(2)	0.40(2)
B'	2*b* (0, 0, $\frac{1}{2}$)	2*b* (0, 0, $\frac{1}{2}$)	4*b* ($\frac{1}{2}$, $\frac{1}{2}$, $\frac{1}{2}$)	1*a* (0,0,0)
B (Å^2)	0.49(5)	0.44(6)	0.37(2)	= Tb B
O1	4*e* (0,0,*z*)	4*e* (0,0,*z*)	24*e* (*x*,0,0)	3*d* ($\frac{1}{2}$, 0, 0)
x	0	0	0.2539(2)	$\frac{1}{2}$
z	0.2665(5)	0.2674(26)	0	0
B (Å^2)	1.33(14)	1.02[a]	1.34(1)	1.25(1)
Occupancy	1.024(36)	1	0.984(4)	0.978(4)
O2	8*h* (*x*,*y*,0)	8*h* (*x*,*y*,0)		
x	0.2441(4)	0.2626(37)		
y	0.2821(4)	0.2470(9)		
z	0	0		
B (Å^2)	1.44(8)	1.12[a]		
Occupancy	1.002(18)	0.986(6)		
R_p (%)	5.5	5.2	5.6	5.5
R_{wp} (%)	6.5	6.6	6.9	7.2
χ^2	2.5	1.8	2.1	2.2

In the partially ordered $x = 0.3$ and 0.6 structures the occupancy of the 2*a* and 4*a* sites, respectively, refines to 74(15)% in the case of $x = 0.3$ and is set as 67% for $x = 0.6$ based on the refinement of the synchrotron X-ray diffraction pattern of this sample.

[a] Oxygen displacement parameters refined anisotropically: O1 $B_{11} = B_{22} = 0.0142(27)$ and $B_{33} = -0.0001(7)$; O2 $B_{11} = 0.0077(35)$, $B_{22} = 0.0099(33)$, $B_{33} = 0.0067(15)$ and $B_{12} = -0.0001(21)$.

gradual loss of *B*-site cation ordering the Tb–O and Sn/Nb–O bonds gradually contract, and expand, respectively with increasing x. There is only a small difference, ≈ 0.03 Å, between the *B*-site cation bond in the disordered structure of the $x = 0.7$ member of the series and the Tb–O and Sn/Nb–O bonds of the last *B*-site ordered compound $x = 0.6$ (see Tables 3 and 4 for refined structures and selected cation distances, respectively). Similarly to the lanthanide cations in $Ba_2PrSn_xSb_{1-x}O_{6-\delta}$, $Ba_2PrSnNb_{1-x}O_{6-\delta}$ and $Ba_2TbSn_xSb_{1-x}O_{6-\delta}$ series the Tb cations are significantly overbonded and the Sn^{4+} and Nb^{5+} cations are significantly underbonded in the structures where these cations occupy the same disordered site.

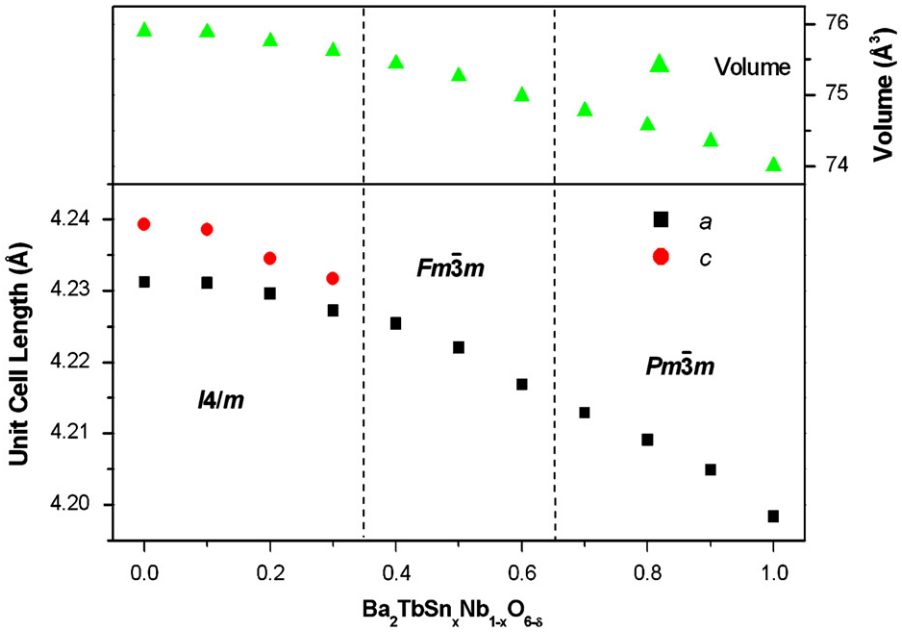

Fig. 5. Reduced unit cell lengths and volumes for compounds in the series $Ba_2TbSn_xNb_{1-x}O_{6-\delta}$.

Table 4
Bond lengths and bond valence sums (BVS) for selected compounds in the $Ba_2TbSn_xNb_{1-x}O_{6-\delta}$ series determined using neutron diffraction

x	Ba–O		Tb–O		B'–O	
	Bond length (Å)	BVS	Bond length (Å)	BVS	Bond length (Å)	BVS
0	4 × 2.884(1) 4 × 2.9941(2) 4 × 3.111(2)	1.84	2 × 2.259(4) 4 × 2.231(3)	3.57	2 × 1.979(4) 4 × 2.011(3)	4.73
0.3	4 × 2.944(9) 4 × 2.993(1) 4 × 3.038(9)	1.81	2 × 2.262(22) 4 × 2.156(20)	4.12	2 × 1.967(22) 4 × 2.075(19)	4.22 4.29
0.6	12 × 2.9829(1)	1.84	6 × 2.142(2)	4.67	6 × 2.076(2)	3.78 3.84
0.7	12 × 2.9797(1)	1.86	6 × 2.1070(1)	5.13	= Tb–O	3.48 3.53

The BVS for Tb is based on the Tb^{3+}–O parameter since the appropriate value for Tb^{4+} is unknown. In the case of the mixed B' compounds the BVS for Sn^{4+} is listed above Nb^{5+}.

Interestingly refinements using a neutron diffraction pattern of the tetragonal $Ba_2TbSn_{0.3}Nb_{0.7}O_{6-\delta}$ sample consistently suggest an unusually large difference between the axial and equatorial Tb–O bond lengths with an axial and equatorial bond length of 2.26(2) and 2.16(2) Å, respectively. This stretching of the axial Tb–O bond is reversed in the Sn/Nb octahedra where the axial bond are significantly shorter than the equatorial bond (cf. 1.97(2)–2.07(2) Å). The cause of these unusually distorted octahedra is not clear although it may be related to the unusually large anisotropic peak broadening observed for (00l) Bragg reflections in the synchrotron X-ray diffraction pattern of both the $x = 0.2$ and 0.3 samples. The larger than expected standard deviations of the oxygen atomic positions, and therefore of the bond lengths in this structure, are caused by cross-correlation between the oxygen atomic positions and the anisotropic displacement parameters used in this model. While the precision of the atomic positions can be greatly increased by using isotropic displacement parameters this also results in noticeably less stable refinements.

3.3. Analysis of oxygen vacancies and oxidation states of cations in $Ba_2LnSn_xNb_{1-x}O_{6-\delta}$

The structures of compounds in the series $Ba_2LnSn_xNb_{1-x}O_{6-\delta}$ (Ln = Pr and Tb) determined in the previous two sections implies that, similar to the analogous $Ba_2LnSn_xSb_{1-x}O_{6-\delta}$ series, as x increases the trivalent lanthanide cations undergo a transition to the tetravalent state [9]. In order to determine the precise way in which this oxidation state change occurs and, therefore, if there is any significant level of oxygen vacancies in these compounds UV-Visible and Near-Infrared and XANES spectroscopies were used to probe the oxidation state of the lanthanide cations in each compound.

The 1200–2200 nm region of the Near-Infrared spectra of Ba_2PrNbO_6 exhibits many sharp peaks similar to those found in Ba_2PrSbO_6 indicating the presence of Pr^{3+} [9,28]. These features lose intensity with increasing x and the broader features found in $Ba_2PrSnO_{6-\delta}$, which are associated with Pr^{4+} [9,29], become more intense (see Fig. 6). This is similar to the trend observed in $Ba_2PrSn_xSb_{1-x}O_{6-\delta}$ [9], suggesting a change in valence state from Pr^{3+} to Pr^{4+}. There are, however, numerous weak features, most notably at 1415 and 1775 nm, in Ba_2PrNbO_6 that increase significantly in intensity towards the midpoint of the series before losing most or all of their intensity in $Ba_2PrSnO_{6-\delta}$. These additional bands were not observed in the analogous antimonates where the Pr^{3+} and Pr^{4+} cations segregate into two distinct phases [9]. We speculate that these bands are a consequence of Pr^{3+}/Pr^{4+} charge transfer.

The 1500–2300 nm region of the spectra of $Ba_2TbSn_xNb_{1-x}O_{6-\delta}$ exhibits a gradual change with increasing x (see Fig. 7). The features found in Ba_2TbNbO_6, while not as strong or sharp as those found in Ba_2TbSbO_6, suggest the presence of Tb^{3+} [9,30,31]. These feature decrease in intensity throughout the series with increasing x leading to a featureless spectra for $Ba_2TbSnO_{6-\delta}$, as

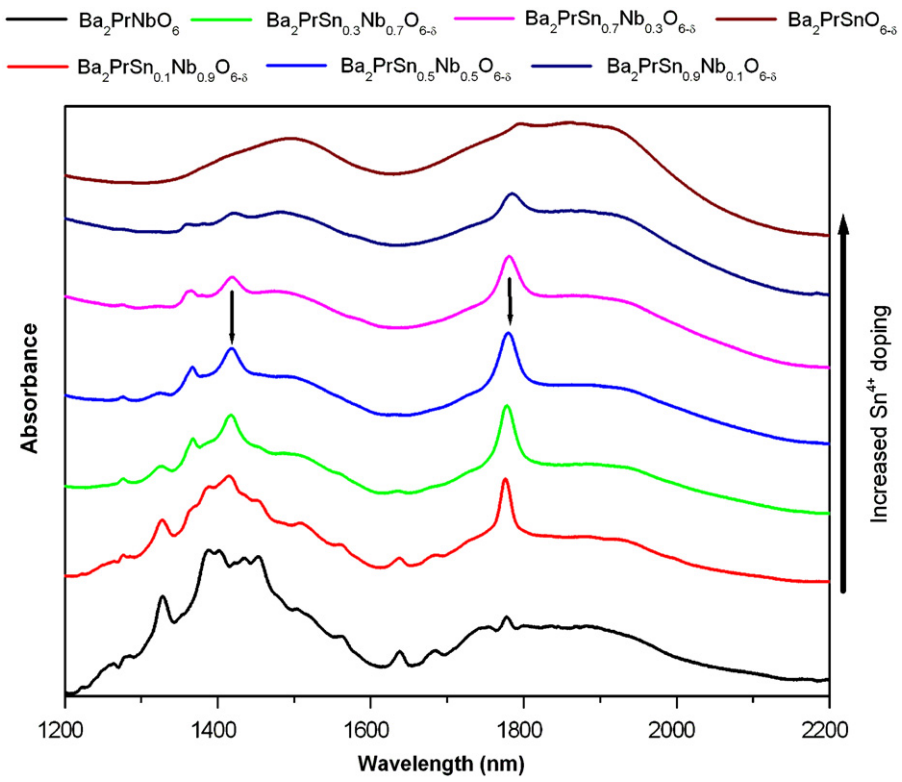

Fig. 6. Selected spectra of compounds in the series $Ba_2PrSn_xNb_{1-x}O_{6-\delta}$ in the region 1200–2200 nm. The peaks marked by arrows in the spectra of $Ba_2PrSn_{0.5}Nb_{0.5}O_{6-\delta}$ at approximately 1415 and 1775 nm are at their most intense in the intermediate compounds.

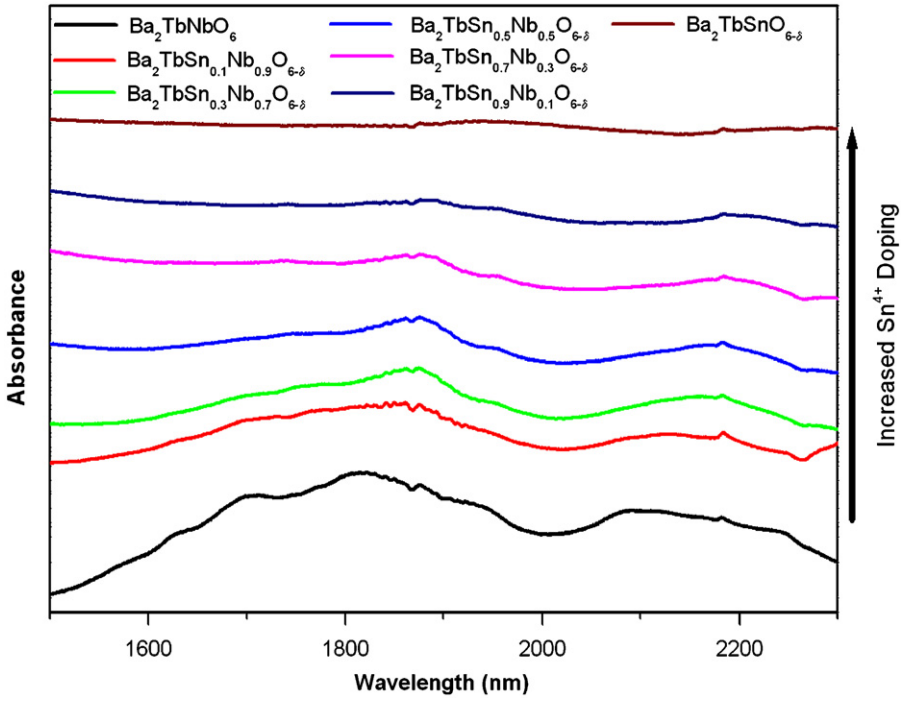

Fig. 7. Selected spectra of compounds in the series $Ba_2TbSn_xNb_{1-x}O_{6-\delta}$ in the region 1500–2300 nm.

noted in a previous study of this compound [9]. This shows that there is a gradual oxidation state change from Tb^{3+} to Tb^{4+} with increased Sn^{4+} doping.

Having used Near-Infrared spectroscopy to confirm that Pr^{3+} and Tb^{3+} cations undergo a valency change to Pr^{4+} and Tb^{4+} in the series $Ba_2LnSn_xNb_{1-x}O_{6-\delta}$ XANES of the Pr and Tb L_{III}-edges were collected in order to quantify the oxidation states of the cations in each compound. The white line of the Pr L_{III}-edge in Ba_2PrNbO_6 occurs at 5.969 keV, which is only 1 eV higher in energy than that of $Pr_2Sn_2O_7$, confirming that Pr is trivalent in this compound.

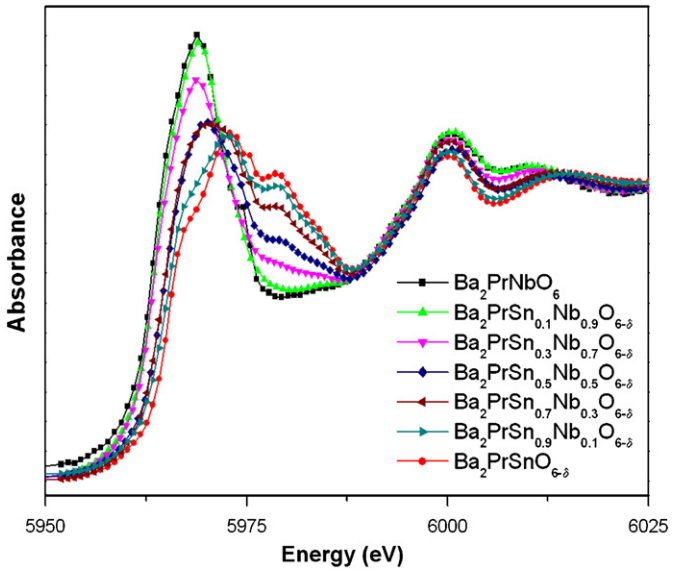

Fig. 8. Pr L_{III}-edge spectra of selected compounds in the series $Ba_2PrSn_xNb_{1-x}O_{6-\delta}$ indicating the change in the energy and shape of the edge between 5960 eV to 5985 eV with increasing Sn^{4+} doping.

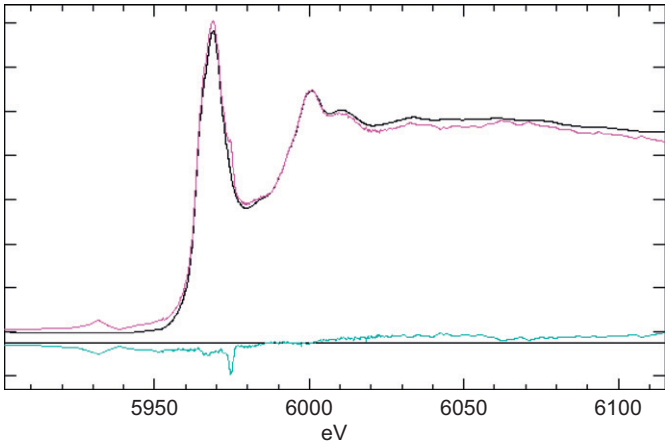

Fig. 9. TARGET fit of the Ba_2PrNbO_6 spectra to the appropriate component of the PCA analysis. The red, black and blue lines are the Ba_2PrNbO_6 and the PCA component spectra and the difference between the two, respectively. Note the extra feature at approximately 5975 eV in the Ba_2PrNbO_6 spectra that is not in the component spectra.

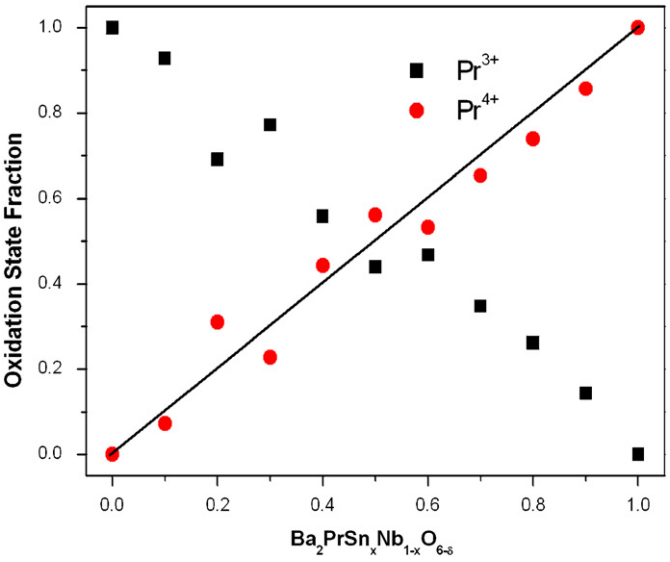

Fig. 10. Plot of the oxidation state fraction of Pr^{3+} and Pr^{4+} in each compound examined in the $Ba_2PrSn_xNb_{1-x}O_{6-\delta}$ series. The black line depicts the amount of Pr^{4+} required at each composition for there to be no oxygen vacancies present and is drawn as a guide to the eye.

These Pr^{3+}-like features decrease in intensity with increased Sn^{4+} doping while features similar to those found in $Ba_2PrSnO_{6-\delta}$ increase in intensity (see Fig. 8). Since it has already been established that the spectra of $Ba_2PrSnO_{6-\delta}$ is consistent with it containing only Pr^{4+} [9] this change demonstrates the oxidation state gradually transforms from Pr^{3+} to Pr^{4+} with increasing x.

Principal component analysis (PCA) indicates that the intermediate compounds in the series $Ba_2PrSn_xNb_{1-x}O_{6-\delta}$ consist of two common components. Target transformation analysis suggests that while one of these is an excellent match to the spectra of $Ba_2PrSnO_{6-\delta}$ the other is not quite as well fitted by Ba_2PrNbO_6 (see Fig. 9). This is principally because of a shoulder at the high-energy side of the white line of Ba_2PrNbO_6. This is not in the spectra of any of the intermediate compounds in the series nor does it match the energy of any Pr^{4+} features in either $Ba_2PrSnO_{6-\delta}$ or $BaPrO_3$. It is therefore believed that it is a spurious artifact caused by an instrumental "glitch" [32,33]. Alternatively it is possible that this feature is caused by a very small amount of an impurity phase found to be present in the sample. This phase has been identified by X-ray diffraction as being Pr_3NbO_7 with Rietveld refinement suggesting that this phase makes up a mole fraction of approximately 1% of the compound. It would seem unlikely, however, that such a small impurity could contribute such a significant feature to the spectra. Despite this issue the L_{III}-edge spectra of Ba_2PrNbO_6 was a significantly better fit to the second PCA component than the $Pr_2Sn_2O_7$ spectra, presumably due to the different co-ordination environment of the Pr^{3+} cations in the perovskite and pyrochlore structure. Therefore Ba_2PrNbO_6 was selected to be used as component of the least squares fit of the spectra of the intermediate samples.

Given that Ba_2PrNbO_6 and $Ba_2PrSnO_{6-\delta}$ have been established by a number of techniques to contain Pr in the trivalent or tetravalent state, respectively, these can be used as Pr^{3+} and Pr^{4+} standards in linear regression analysis of the spectra of the intermediate compounds in the series $Ba_2PrSn_xNb_{1-x}O_{6-\delta}$. The multiple linear regression analysis of the spectra of intermediate compounds in the series showed that the Pr^{3+} is progressively replaced by Pr^{4+} with increased Sn^{4+} doping. There is no evidence for a significant level of oxygen vacancies in these compounds (see Fig. 10 and Table 5 for oxidation state fractions and oxygen stoichiometry, respectively). It should be noted, however, that the fraction of Pr in each oxidation state does not change as smoothly as was found for either of the antimonate series [9]. This is most likely related to the additional feature in the Ba_2PrNbO_6 spectra causing complications in the fitting process and decreasing the accuracy of the results.

The edge in the Tb L_{III}-edge spectra of Ba_2TbNbO_6 occurs at a very similar energy to that of the Tb^{3+} standard, $Tb_2Sn_2O_7$. The edge does not have any features in the range of the Tb^{4+} standard, $BaTbO_3$, showing that only Tb^{3+} is present. This is consistent with other results obtained for this compound. XANES shows that only Tb^{4+} is present in $Ba_2TbSnO_{6-\delta}$ [9] illustrating the oxidation state changes fully from Tb^{3+} to Tb^{4+} with increasing Sn^{4+} doping. The spectra of the intermediate compounds illustrates that this change occurs gradually (see Fig. 11).

A combination of PCA and target transformation analysis showed that the intermediate compounds in the series

Table 5
Oxygen stoichiometry as determined by the least squares fit of the Pr and Tb L_{III}-edges for perovskites in the series $Ba_2LnSn_xNb_{1-x}O_{6-\delta}$ (Ln = Pr or Tb)

$Ba_2LnSn_xSb_{1-x}O_{6-\delta}$	Oxygen stoichiometry	
x	Pr	Tb
0	6.00(1)	6.00(1)
0.1	5.99(1)	5.98(1)
0.2	6.05(3)	5.98(1)
0.3	5.96(1)	5.99(1)
0.4	6.02(2)	5.98(1)
0.5	6.03(1)	5.98(1)
0.6	5.97(1)	5.97(1)
0.7	5.98(1)	5.98(1)
0.8	5.97(1)	5.97(1)
0.9	5.98(1)	5.97(1)
1.0	6.00(1)	6.00(1)

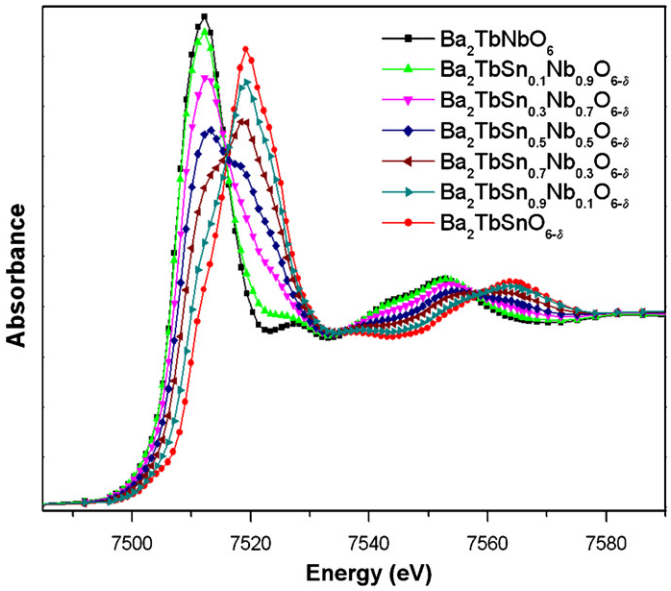

Fig. 11. Tb L_{III}-edge spectra for selected compounds in the series $Ba_2TbSn_xNb_{1-x}O_{6-\delta}$ indicating the change in shape and energy of the edge with increasing x.

$Ba_2TbSn_xNb_{1-x}O_{6-\delta}$ consist of only two common components. These components are excellent fits for the spectra of the two end-member compounds, Tb^{3+} containing Ba_2TbNbO_6 and Tb^{4+} containing $Ba_2TbSnO_{6-\delta}$. A multiple linear regression analysis of each of these intermediates was carried out using these two component spectra. This analysis indicates that the rate of the Tb oxidation state change as Sn^{4+} doping increases results in a very small amount of oxygen vacancies, $\delta \approx 0.02$, being maintained in each of the intermediate compounds (see Fig. 12 and Table 5 for oxidation state fraction and oxygen stoichiometry, respectively). Since approximately the same amount of oxygen vacancies are found in each intermediate compound in this series it is considered likely that they are present despite the quantity being only twice the experimental error. The presence of a small amount of oxygen vacancies in compounds in the series $Ba_2PrSn_xNb_{1-x}O_{6-\delta}$ is similar to the observation of oxygen vacancies in the series $Ba_2TbSn_xSb_{1-x}O_{6-\delta}$ although the lightly doped Sn^{4+} compounds in the antimonate series were found to have more oxygen vacancies with a maximum $\delta \approx 0.05$ being found for samples with $x = 0.1$–0.3 [9]. The analysis of the

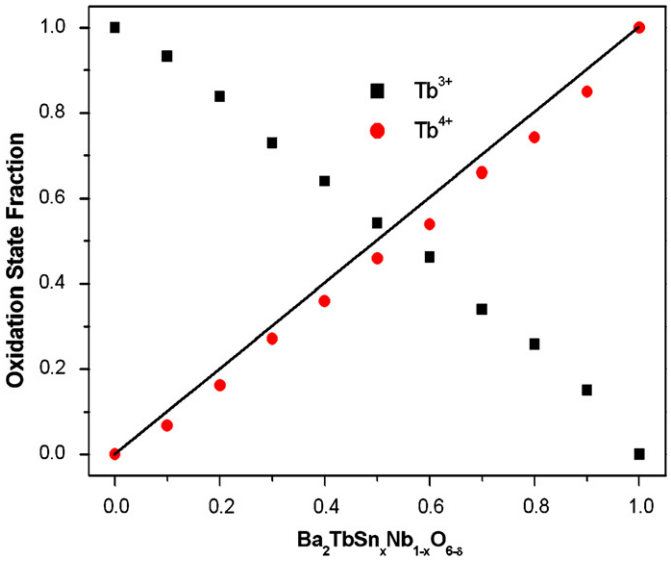

Fig. 12. Plot of the oxidation state fraction of Tb^{3+} and Tb^{4+} in each compound examined in the $Ba_2TbSn_xNb_{1-x}O_{6-\delta}$ series. The black line depicts the amount of Tb^{4+} required at each composition for there to be no oxygen vacancies present and is drawn as a guide to the eye.

$Ba_2PrSn_xB'_{1-x}O_{6-\delta}$ ($B' = Nb^{5+}$ or Sb^{5+}) series on the other hand did not reveal any significant level of oxygen vacancies through a significant part of the series. In part, this may simply be a result of the larger error in the least squares analysis of the $Ba_2PrSn_xNb_{1-x}O_{6-\delta}$ series obscuring the presence of such vacancies.

4. Conclusions

The compounds in the series $Ba_2LnSn_xNb_{1-x}O_{6-\delta}$ (Ln = Pr or Tb) have been synthesised and characterised using a combination of synchrotron X-ray and neutron diffraction, Near-Infrared and XANES spectroscopies. It was found that the niobate end-members of the series had double perovskite structures with full B-site ordering, in $I2/m$ monoclinic and $I4/m$ tetragonal for the Pr^{3+} and Tb^{3+} compounds, respectively. This contrasts with the lack of B-site ordering in the $x = 1.0$ members of the series. As previously found in the $Ba_2LnSn_xSb_{1-x}O_{6-\delta}$ series the loss of B-site ordering with increasing x is related to the oxidation state of the lanthanides changing gradually from the trivalent state in the $x = 0$ compounds to the tetravalent state in the $x = 1.0$ compounds.

Unlike the analogous antimonate series the $Ba_2PrSn_xNb_{1-x}O_{6-\delta}$ compounds show no sign of cation segregation indicating that Pr^{3+} and Pr^{4+} occupy the same structure. Variable temperature X-ray diffraction shows that the two-phase region in this series, between $x = 0.2$ and 0.4, is caused by a discontinuous phase transition between the $I2/m$ monoclinic and $R\bar{3}$ rhombohedral symmetries. The loss of B-site cation ordering occurs abruptly between $x = 0.7$ and 0.8, which is different from both the terbium niobate and antimonate series where the loss of B-site cation ordering occurs gradually with increasing x. Least squares analysis of the Pr XANES spectra suggests that none of the Pr compounds contain a significant level of oxygen vacancies. A similar analysis of the Tb XANES spectra reveals that compounds in the terbium series may contain a small amount of oxygen vacancies although this is noticeably less than that found in the analogous antimonate series.

Acknowledgments

This work has been partially supported by the Australian Research Council and the Australian Institute of Nuclear Science and Engineering (AINSE) through the provision of an AINSE Postgraduate Award. The work performed at the Australian National Beamline Facility was supported by the Australian Synchrotron Research Program under the Major National Research Facilities Program. The X-ray diffraction patterns obtained at the ANBF were collected with the help of Dr. James Hester. The authors would like to thank Dr. Hugh Harris for his advice regarding analysis of the XANES spectra.

Disclaimers

Commercial Product Disclaimer: The identification of any commercial product or trade name does not imply endorsement or recommendation by the National Institute of Standards and Technology.

Appendix A. Supplementary Materials

Supplementary data associated with this article can be found in the online version at doi:10.1016/j.jssc.2008.07.021.

References

[1] R.H. Mitchell, Perovskites Modern and Ancient, Almaz Press Inc., Ontario, 2002.
[2] V.V. Kharton, F.M.B. Marques, A. Atkinson, Solid State Ion. 174 (2004) 135–149.
[3] J.B. Goodenough, Rep. Prog. Phys. 67 (2004) 1915–1993.
[4] S.J. Skinner, Int. J. Inorg. Mater. 3 (2001) 113–121.
[5] K.D. Kreuer, Solid State Ion. 97 (1997) 1–15.
[6] T. Ishihara, H. Matsuda, Y. Takita, J. Am. Chem. Soc. 116 (1994) 3801–3803.
[7] N. Bonanos, K.S. Knight, B. Ellis, Solid State Ion. 79 (1995) 161–170.
[8] P. Murugaraj, K.D. Kreuer, T. He, T. Schober, J. Maier, Solid State Ion. 98 (1997) 1–6.
[9] P.J. Saines, B.J. Kennedy, M.M. Elcombe, H.H. Harris, L.-Y. Jang, Z. Zhang, J. Solid State Chem., in press, doi:10.1016/j.jssc.2008.07.007.
[10] R.D. Shannon, Acta Crystallogr. A 32 (1976) 751–767.
[11] A.M. Glazer, Acta Crystallogr. A 31 (1975) 756–762.
[12] A.M. Glazer, Acta Crystallogr. B 28 (1972) 3384–3392.
[13] P.J. Saines, B.J. Kennedy, M.M. Elcombe, J. Solid State Chem. 180 (2007) 401–409.
[14] P.J. Saines, J.R. Spencer, B.J. Kennedy, Y. Kubota, C. Minakata, H. Hano, K. Kato, M. Takata, J. Solid State Chem. 180 (2007) 3001–3007.
[15] T.M. Sabine, B.J. Kennedy, R.F. Garrett, G.J. Foran, D.J. Cookson, J. Appl. Crystallogr. 28 (1995) 513–517.
[16] C.J. Howard, C.J. Ball, R.L. Davis, M.M. Elcombe, Aust. J. Phys. 36 (1983) 507–518.
[17] B.A. Hunter, C.J. Howard, A Computer Program for Rietveld Analysis of X-ray and Neutron Powder Diffraction Patterns, Lucas Heights Laboratories, 1998.
[18] R.J. Hill, J. Appl. Crystallogr. 25 (1992) 589–610.
[19] H.G. Scott, J. Appl. Crystallogr. 16 (1983) 159–163.
[20] B.J. Kennedy, B.A. Hunter, C.J. Howard, J. Solid State Chem. 130 (1997) 58–65.
[21] M. Yoshimura, T. Nakamura, T. Sata, Bull. Tokyo Inst. Technol. 120 (1974) 13–27.
[22] Y. Hinatsu, J. Alloys Compd. 193 (1993) 113–115.
[23] G.N. George, I.J. Pickering, EXAFSPAK: A Suite of Computer Programs for Analysis of X-ray Absorption Spectra, Stanford Synchrotron Radiation Laboratory, 2000.
[24] P.J. Saines, B.J. Kennedy, J. Solid State Chem. 181 (2008) 298–305.
[25] B.J. Kennedy, C.J. Howard, K.S. Knight, Z. Zhang, Q. Zhou, Acta Crystallogr. B 62 (2006) 537–546.
[26] V.F. Sears, Neutron News 3 (1992) 26–37.
[27] V. Ting, Y. Liu, R.L. Withers, L. Norén, M. James, J.D. Fitz Gerald, J. Solid State Chem. 179 (2006) 551–562.
[28] D.A. Pawlak, T. Lukasiewicz, M.A. Carpenter, M. Malinowski, R. Diduszko, J. Kisielewski, J. Cryst. Growth 282 (2005) 260–269.
[29] D. Pawlak, Z. Frukacz, Z. Mierczyk, A. Suchocki, J. Zachara, J. Alloys Compd. 275–277 (1998) 361–364.
[30] L. Ning, C.S.K. Mak, P.A. Tanner, Phys. Rev. B 72 (2005) 085127.
[31] V.F. Zolin, J. Alloys Compd. 380 (2004) 101–106.
[32] G.G. Cohen, D.A. Fischer, J. Colbert, N.J. Shevchik, Rev. Sci. Instrum. 51 (1980) 273–277.
[33] F. Bridges, X. Wang, J.B. Boyce, Nucl. Instrum. Meth. A 307 (1991) 316–324.